Formation, breaching and flood consequences of a landslide dam near Bujumbura, Burundi

Léonidas Nibigira[1], Hans-Balder Havenith[1], Pierre Archambeau[2], and Benjamin Dewals[2]

[1]Geohazards and Environment, Department of Geology, University of Liege, 4000 Liege-Belgium

5   [2]Hydraulics in Environmental and Civil Engineering (HECE), Research unit Urban & Environmental Engineering, University of Liege, 4000 Liege-Belgium

Correspondence to: Léonidas Nibigira (leonidas.nibigira@doct.ulg.ac.be)

Abstract. This paper investigated the possible formation of a landslide dam on the Kanyosha River near Bujumbura, the capital of Burundi, as well as the interplay between the breaching of this landslide dam and the flooding along the river. We present

10   an end-to-end analysis, ranging from the origin of the landslide up to the computation of flood waves induced by the dam breaching. The study includes three main steps. First, the mass movement site was investigated with various geophysical methods that allowed us to build a general 3D model and detailed 2D sections of the landslide. Second, this model was used for dynamic landslide process modelling with the Universal Distinct Element Code. The results showed that a fifteen-meter-high landslide dam may form on the river. Finally, a 2D hydraulic model was setup to find out the consequences of the

15   breaching of the landslide dam on flooding along the river, especially in an urban area located downstream. Based on 2D maps of maximum water depth, flow velocity and wave propagation time, the results highlight that neglecting the influence of such landslide dams leads to substantial underestimation of flood hazard in the downstream area.

Keywords Bujumbura, landslide dam, dam breaching, geomechanic and hydraulic modelling, flood propagation, multi-hazard

1   Introduction

20   The city of Bujumbura faces serious problems related to natural hazards. Recurrent floods induced by heavy rains cause tremendous losses. The damage can be even much higher in case of multiple hazard interactions. This was the case in February 2014, when the flood resulting from a failure of a temporarily created landslide dam caused 64 casualties. Over 940 houses were destroyed and this resulted in over 12,500 homeless people (UNITAR/UNOSAT 2014, Reliefweb 2014). Floods due to land instabilities and steep slopes in the Great Lakes of Africa region were reported by Ilunga (2006) who studied the problem

25   of debris flows caused by river overflows and soil erosion in the area of Uvira (Democratic Republic of Congo). Moeyersons et al. (2010) also mentioned temporary landslide barriers that can contribute to irregular river hydrographs in the region. However, studies providing quantified scenario analyses are still missing. The lack of multi-risk studies in equatorial Africa was highlighted recently by Jacobs et al. (2016). In order to assess the interactions between landslides and rivers, we studied the existing mass movement called 'Banana Tree Landslide' (called BTL below) that, due to its geographic location, represents

30   a major risk for the city of Bujumbura. As shown in Fig. 1, the 'Banana Tree landslide' is located on the south slope of the Kanyosha River valley. The Kanyosha watershed area is 59.4 km^2 and the catchment upstream the BTL has 51.3 km^2. The Kanyosha River has its source in the high mountains of the Congo-Nile crest in the East as mentioned in Fig. 1. Therefore, the watershed has steep slopes especially in the rural areas, which are susceptible to large instabilities. Thus, the volume of the BTL is estimated at more than 5×10^6 m^3 (see general view in Fig. 2a); the average overall width of the landslide in the east-

35   west direction is 500 m.
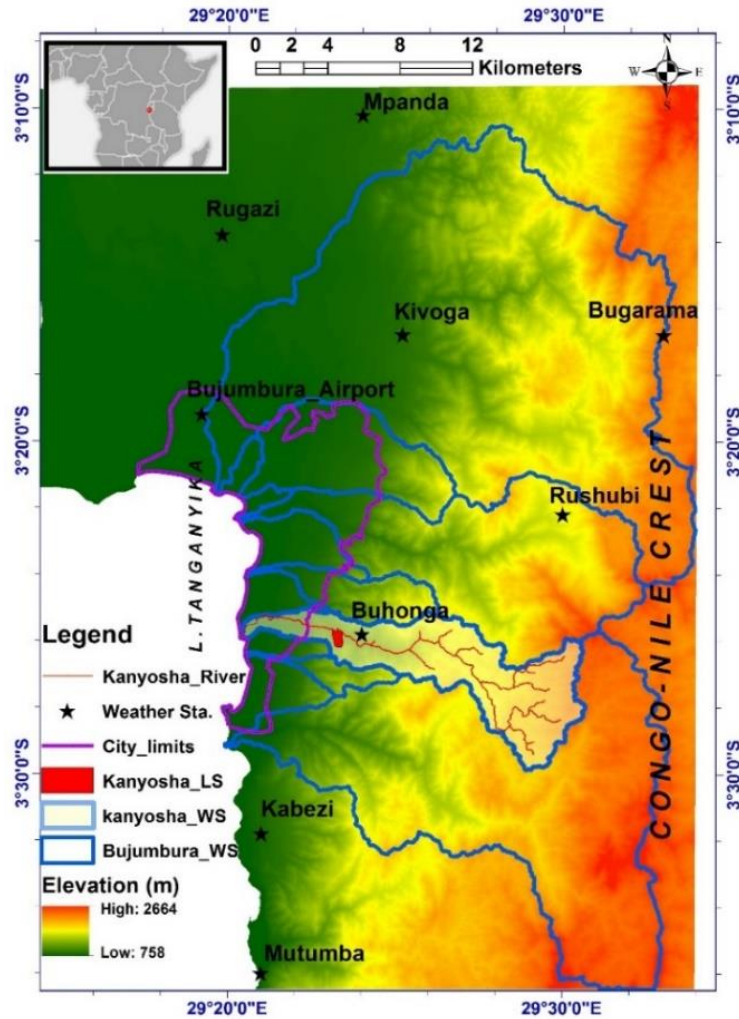
Figure 1. Map of Bujumbura region (city outlined in violet) with indication of watersheds for the main rivers (blues contours), the limits of the city and the Lake Tanganyika. The watershed of the Kanyosha River is highlighted in the central part, with the river network (red lines) inside. The weather stations in and around Bujumbura (black star), the Kanyosha Landslide (in the text called 'Banana Tree Landslide', sometimes referred to as BTL, in red contours) and the Congo- Nile crest are also shown. 'LS' and 'WS' stand for Landslide and Watershed.

40
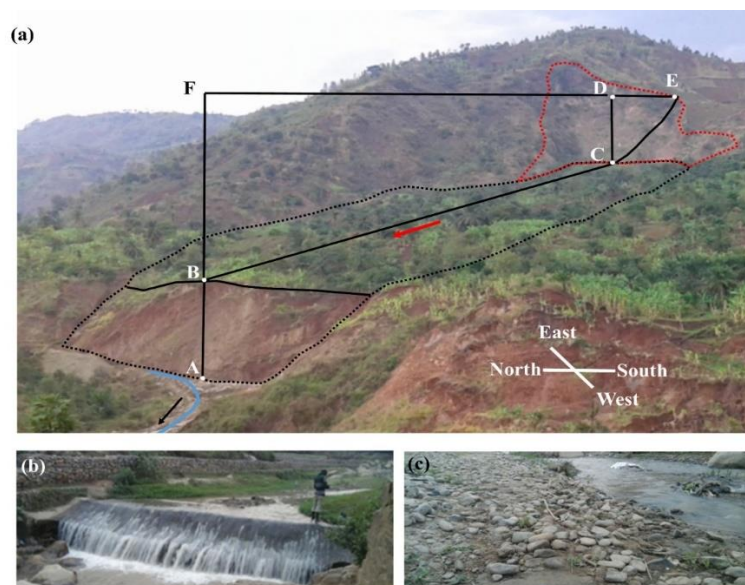
Figure 2. (a) Downstream view of BTL (black dotted contour) and the main scarp (red dotted contour). Landslide sliding direction (red arrow) and the river flow direction (black arrow) are indicated by arrows. AB, BC and CD indicate the height of the scarp on the river cross section at the foot of the BTL (AB = 26 m), the BTL length in the sliding direction (BC = 750 m) and the main scarp height (CD = 75m). The blue line indicates the river channel axis. (b) Waterfall over a destroyed old hydraulic structure. (c) View of the river bed showing dry season water path and the bed grains size in the area occupied by water only during rainy seasons.

Our recent observations show that the western part of the landslide (in the foreground of Fig. 2a), with relatively soft slopes, is marked by very local slope instabilities that do apparently not contribute to the general movement. However, the eastern part (black dot outlines), with steep slopes downstream near the river and an average width of 250m, is very active and could soon move and form a landslide dam. The presence of water ponds in this eastern parts (view shown at the end of this paper in Fig. 14) is likely to contribute to future instability that could develop along the main sliding axis BC (shown in Fig. 2a). The position of that landslide upstream of the southern part of the city makes it an imminent danger for life and for the country's economy. In order to understand the landslide mechanisms in terms of triggering factors, evolution and effects, numerical modelling has been carried out to analyse its stability, also under dynamic (seismic) conditions. The effects of the dam and its breaching on the flood potential along the river and the consequences especially downstream in the urban area were studied through an additional hydraulic model.

2 Data and methods

2.1 Channel description

The riverbed material of Kanyosha River has a variable grain size, which can be classified into three main groups. The first group consists of small pebbles of around 10 cm in diameter (Fig. 2c). The diameter of this category rarely reaches 40 cm. The second group is made up of large and isolated stones that are often prone to the action of humans, carving them into building materials. This category is difficult to take into account due to its strong irregularity. The third group consists of sludge accumulation zones and debris, especially in the downstream part of the river. In this category, we can mention small

herbaceous islets, often located on minor parts of the bed rarely occupied by water during low water periods. As in the second group, this category is found only in small isolated and scattered areas. Globally, the first group remains hydraulically predominant. Here, the variability of the grain size was accounted for by means of sensitivity analysis (Sec. 3.3).

In 2006, hydraulic structures were constructed to regulate the river; but they were quickly damaged by floods during the following raining seasons. Nonetheless, isolated pebbles resulting from the destruction of these structures are observed. They join the second group described above. The accumulation of material upstream of the remains of the structures often form horizontal platforms, generating small waterfalls (Fig. 2b).

2.2 Topographic and geophysical data

We used a 10 m–resolution Digital Elevation Model (DEM) of the river valley, provided in the coordinate system UTM35S and in raster format. It was produced in 2012 by the '*Bureau de Centralisation Geomatique du Burundi*'. Here, it was resampled at a resolution of 2 m × 2 m, which is the resolution used for hydraulic modelling. For the second part of the analysis, the geometry of the dam was incorporated, taking into account the results provided by the first part related to the landslide process analysis. Given that no data were available for defining the river bathymetry, the flow was computed based on the DEM.
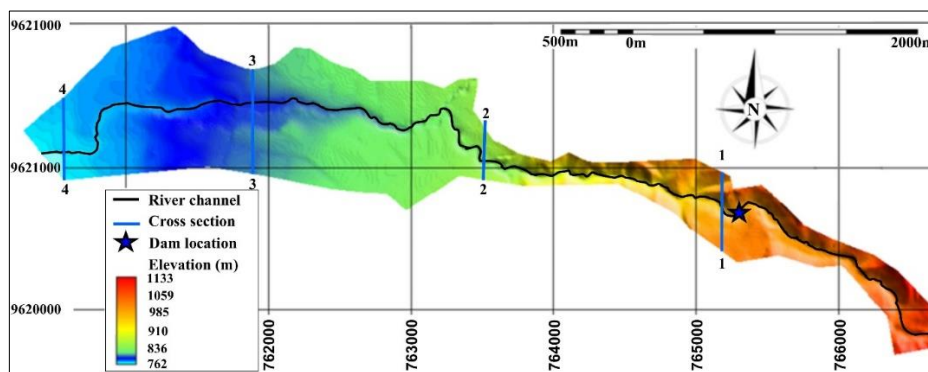
Figure 3. Shaded digital elevation model (m) used for hydraulic modelling within the computation domain with cross sections where hydrographs were extracted (blue lines) and dam location (blue star with black outline). The river channel (black line) is also highlighted.

For the landslide stability analysis, the surface data provided by the DEM were combined with subsurface information obtained by local geophysical field measurements completed in summer 2013. They consist in electrical resistivity tomography (ERT) and ambient noise HV measurements. Fig. 4 provides an overview of the measurements and two examples of ERT profiles. From these investigations, the thickness of the landslide mass and some of its geophysical properties (notably, the elastic properties) could be determined.
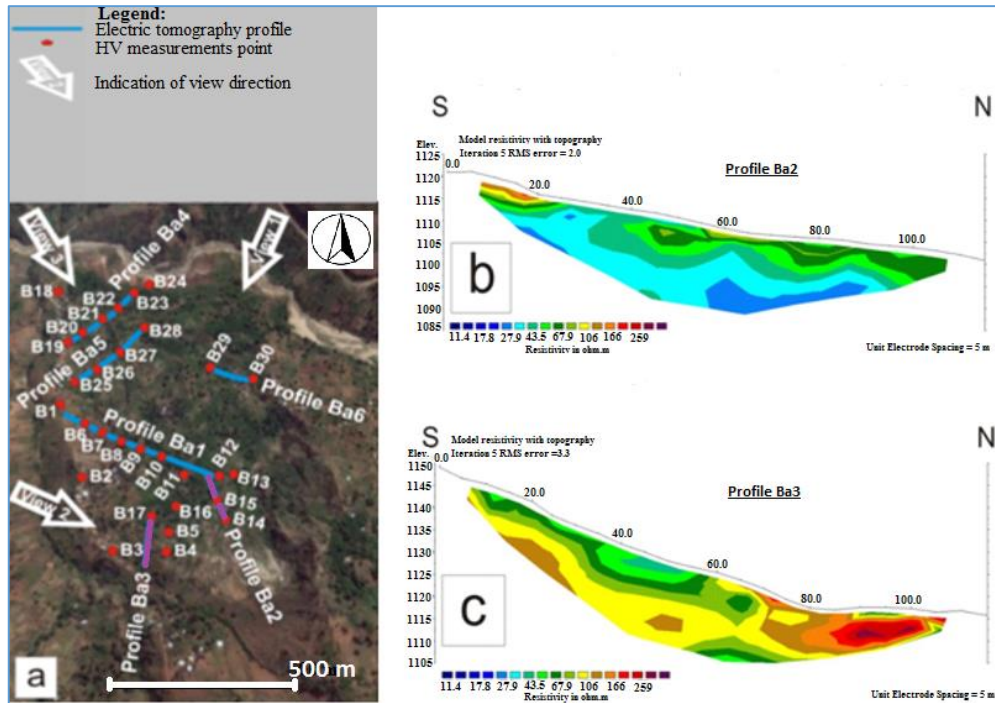
Figure 4. The 'Banana Tree Landslide' field measurements: overview of ERT and HV measurement locations (a), ERT profiles Ba2 (b) and Ba3 (c). In Fig. 4a, Ba2 and Ba3 profiles are highlighted in purple.

2.3 Landslide analysis with UDEC: model construction

The slope stability analysis and mass movement modelling were carried out in 2D using the Universal Distinct Element Code (UDEC). UDEC was developed by Cundall (1971) to evaluate the response of materials (discretized as blocks) to a given loading in static and dynamic (e.g. seismic) conditions. The distinct element method has been used in various studies and it is particularly suitable for rock slope stability analyses (Kveldsvik et al., 2009, Kainthola et al., 2012, Bhasin and Kaynia 2004, Esaki et al., 1999, Chuhan et al., 1997).

From the field measurements, a model of the landslide was established. Fig. 5 corresponds to a 2D section along the main axis of the mass movement and shows the present (actual) topography of the landslide (plain line) and the reconstructed (estimated) initial topography (before first instabilities appeared, marked by a dashed line) as well as the main sliding surface (dotted line). The initial situation is characterized by an average slope of about 15° while the current profile (red line) is marked by a clear scarp in the upper part, below which the landslide material has a thickness of about 15 m and by more massive landslide deposits (thickness of about 50 m) in the middle and the lower part towards the river.
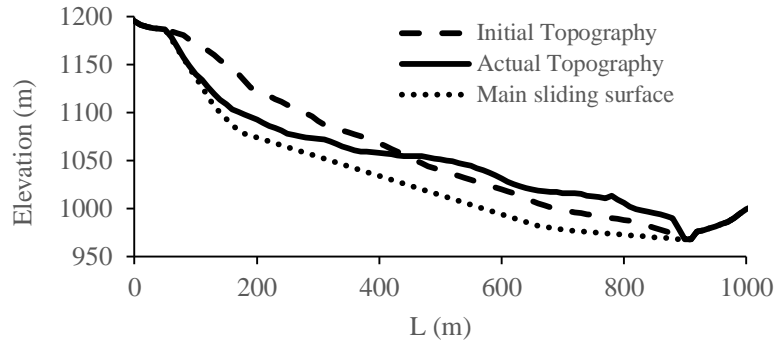
Figure 5. Initial and present BTL profiles. The larger thickness of the present profile in the downstream part of the model is a result of the relative lift-up after a trans-rotational sliding and material accumulation from the upper parts of the initial profile.

For the modelling with UDEC, the landslide was subdivided into three main blocks (see numerical measurement points 12, 13, 15, in Fig. 6, which are located on the upper, middle and lower block, respectively). Cracks (joints) included between the blocks (that represent also main geomorphic and geophysical units observed in the field) allow for the simulation of a more flexible movement of the mass. The same material (material 1 in Table 1) was attributed to all landslide blocks. It corresponds to the average type of the material found within the landslide. Material 2 was attributed to the stable bedrock (Table 1 and Fig. 6).
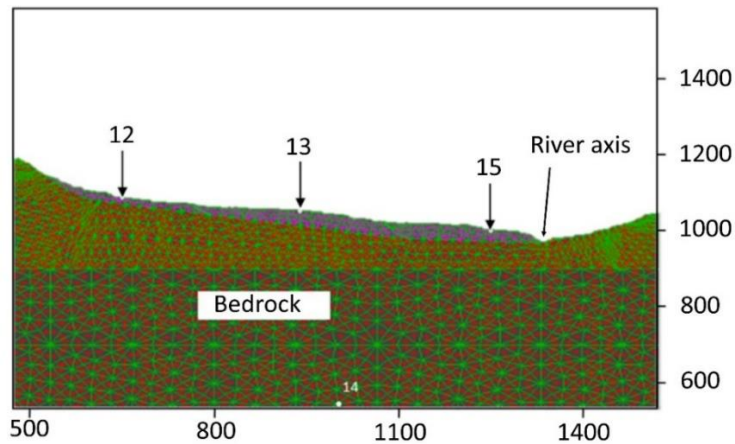
Figure 6. Materialization of blocks, joints and materials for the actual model. The history (measurement) points 12, 13 and 15 (white dots) located, respectively, on the upper, middle and lower block correspond to the surface area where parameters were monitored (e.g. the *x*-acceleration). The point 14 is located at the basis of the model, within the bedrock. The axis of the Kanyosha River is located to the right of the history point 15.

The block materials were considered as purely elastic; therefore, the plastic deformation was only computed along joints. For the block materials the following properties were defined: dry density(ρ), Young's modulus (E), bulk modulus (K) and shear modulus (G), Poisson's ratio (ν), (elastic properties determined on the basis of the estimated and locally measured P-wave velocity, Vp and S-wave velocity, Vs).

Table 1. Parameters used for the blocks properties

Location	Vp (m s^{-1})	Vs (m s^{-1})	ν	ρ (kg m^{-3})	E (GPa)	K (MPa)	G (MPa)	Material
Sliding blocks	1800	800	0.38	2200	3.88	5250.67	1408	1
Bedrock	2600	1400	0.30	2500	12.27	10366.67	4900	2

To allow for plastic deformation along the joints, it is necessary to define the cohesion and the friction angle for the joint/contact material between the blocks. Plastic contact materials were used along the sliding surface and between the blocks (joint material
125   1); for other (auxiliary) contacts, joint material 2 was used, which only allows for elastic deformation.

Table 2. Contact properties: applied values for normal stiffness (jkn), tangential stiffness (jks), range of used cohesion values (jcoh), range of used friction angle values (jfric) and permeability (jperm)

Contact material	jkn (Pa m^{-1})	jks (Pa m^{-1})	jcoh (MPa)	jfric (^{0})	jperm
Joint material 1	1000	10000	0.01-0.05	10-20	0
Joint material 2	1000	10000	2.00E+20	2.00E+20	0

Scenarios were prepared based on the knowledge of the landslide triggering and evolution factors. Those scenarios were
130   preceded by a back-analysis as the pre-slide topography was used as starting point. Calculations first targeted the reproduction
of the present situation of the mass movement before simulating future possible evolutions of the landslide, including the
formation of a dam. Variable factors are related to slope geometry, slope material strength, hydrogeological conditions,
structural discontinuity, weathering, development of weak zones, lithology and earthquakes (those variables were selected
according to those used by published works, such as by Bhasin and Kaynia, 2004, Umrao et al., 2011, Singh et al., 2013a,
135   Kainthola et al., 2012 and Sharma et al., 2017). As major triggering factor, the variable groundwater level was modelled.
Further, to test the possible seismic influence on initial slope stability and the possible future evolution of the landslide, a
synthetic earthquake signal was used as input for some models. Actually, a partial contribution of earthquake shaking to the
destabilization of the slope is highly probable as the site is located in a seismically active area (see last seismic hazard maps
of the Western Branch of the East African Rift by Delvaux et al., 2016). As seismic input we used a Ricker wavelet with
140   maximum amplitude of 0.105 g (about 1.05 m s^{-2}) and central frequencies of 0.5 and 1.4 Hz. The loading was varied in terms
of changing shaking duration. Four different values were considered: 14 seconds, 17 seconds, 25 seconds and 51 seconds.
Figure 7 provides the corresponding signals.
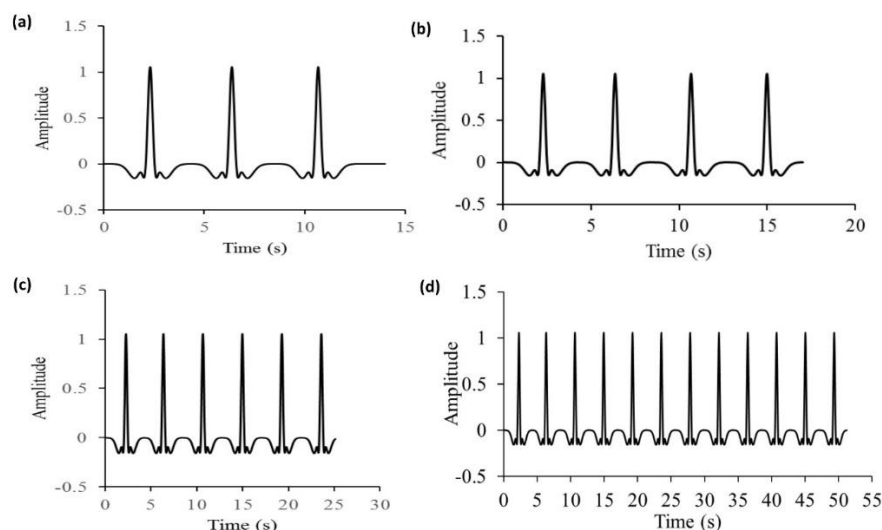
Figure 7. Four signals of changing duration and composed of Ricker wavelets (here with normalized amplitude), corresponding to: 14 s (a), 17 s (b), 25 s (c) and 51 s (d), were used as seismic inputs.

The effects of groundwater level were studied considering 5 different cases: no groundwater (dry scenario), saturation of the whole profile (GWT4), groundwater level at a depth of 15 m in the upper block and the saturation of the middle and lower blocks (GWT5), and finally, the groundwater at a regular depth of 7 m below the surface (GWT6). Results discussed in this paper derive from a set of 52 scenarios given in Appendix A (Fig. A1).

2.4   Hydraulic modelling

For the hydraulic analysis, we used the academic model WOLF 2D, which solves the shallow-water equations by means of a stable and conservative finite volume scheme. This model has been extensively validated and applied for simulating flow induced by dam and dike breaching (Dewals et al., 2011; Roger et al., 2009) as well as for conducting flood risk analysis (Arrault et al., 2016; Beckers et al., 2013; Bruwier et al., 2015; Detrembleur et al., 2015; Ernst et al., 2010). We detail below how friction was parametrized in the hydraulic model, as well as the prescribed boundary conditions and the modelling procedure.

2.4.1 Parametrization of friction

In the hydraulic model, flow resistance was parametrized using the formulation developed by Machiels et al. (2011). Compared to more standard friction formulae (e.g., Manning, Chezy), it offers two main advantages: *(i)* being truly physically-based, it reduces substantially the need for recalibrating the model when the range of flow rate is varied; *(ii)* the only parameter to be set is the characteristic size of bottom irregularities, which can be estimated from field observations. This parametrization is hence particularly suitable for applications for which only scarce flow monitoring data are available, such as in the present case.

Here, we tested three values for the roughness height: 0.1 m, 0.2 m and 0.3m, corresponding to the prevalent class of grain size in the riverbed material (as described in section 2). In the following, to show the effects of the roughness of the river bed, we present the results for the two extreme values of the roughness height ($k_s = 0.1$ m and $k_s = 0.3$ m).

2.4.2 Hydraulic boundary conditions and computed scenarios

The upstream boundary condition is a prescribed flow hydrograph, representing either a flood wave coming from the upstream catchment or a steady inflow. As detailed in Sec. 2.4.3 and in Appendix B, we used only steady inflows, corresponding respectively to a base flow (3 m³ s⁻¹), a 20-year flood (peak discharge of 60 m³ s⁻¹) and a 50-year flood (peak discharge of 120 m³ s⁻¹).

At the downstream end of the computational domain, the river mouth in Lake Tanganyika was not included explicitly because only limited information was available on bathymetric and hydraulic data at this location. Consequently, the hydraulic behaviour of the river mouth is lumped into the boundary condition prescribed at the downstream end of the computational domain. The proposed boundary condition is based on a weir equation, relating the outflow discharge Q_o to the averaged water level h_o close to the simulation downstream boundary:

$$Q_0 = \frac{2}{3} C_D L \sqrt{2g(h_0 - w)} \tag{1}$$

with g being the gravity acceleration (m s⁻²), C_D a non-dimensional discharge coefficient (taken equal to 0.75), L an equivalent crest length (m) and w an equivalent crest height (m). Equation (1) enables simulating different configurations (e.g., loosely vs. strongly varying downstream water level when the flow rate changes) and we performed a sensitivity analysis by varying L and w. For very high values of L, h_o remains virtually constant whatever Q_o; otherwise it varies with Q_o. However, as shown in Appendix C, this boundary condition has actually an influence only over a very limited distance upstream of the domain boundary: in all the conducted tests, this influence zone did not extend over more than 300 meters. This very limited influence results from the relatively steep slope of the river (around 1.5 % in the downstream area; 6 % in the upstream reach). Consequently, the particular formulation of the downstream boundary condition (Eq. (1)) can be safely disregarded when analysing the modelling results over virtually the whole computational domain (except the most downstream 300 m) since they remain independent L and w.

2.4.3 Modelling procedure

The modelling procedure involves two steps (Dewals et al., 2011).
- First, a pre-failure flow is computed in the river (steady flow corresponding to the mean discharge in the river, or to a typical long-duration flood). In this step, the dam geometry is incorporated in the topographic data used for flow computation. This means that the dynamics of material sliding into the river is not reproduced in the hydraulic modelling.
- Second, using the result of step 1 as initial condition, the flow induced by the breaching of the dam is computed.

As it is not possible to anticipate when the landslide dam breaching might occur, we consider three different pre-failure flow conditions: base flow, 20-year flood and 50-year flood.

2.5   Flood hazard mapping methodology

The results of the hydraulic computations were processed to display the inundation extent as well as information on water depth and flow velocity in the floodplains. The method used by Alvarez et al. (2017) was considered for the classification of flood hazard in high, medium and low categories. To be classified in the high category, the location must have a water depth higher than 1 m, a water velocity greater than 1 m s⁻¹ or a product of the velocity and the water depth greater than 0.5 m s⁻².

Conditions to be classified in the category of low flood hazard are: a water height below 0.5 m, a flood velocity below 0.5 m s^{-1} and a product of the velocity and the water depth below 0.25 m s^{-2}. The medium hazard category consists in the intermediate situation.

3   Results

3.1   Landslide triggering: back analysis

205

The results obtained from the elastic model with initial topography (scenarios 1 and 2 in Appendix A, Fig. 15a) were first measured in terms of peak ground acceleration (PGA) and Arias Intensity (Ia, see Arias, 1970) in different parts of the profile. This was calculated from the acceleration recorded in x-direction for specific history points chosen within the model profile. Figure 8 and Table 3 provide x-acceleration, PGA and Ia for the upper and for the lower blocs considering 14 seconds and 25 seconds. As we were interested in finding how the landslide was triggered and evolved, we tracked the upper block displacement and its detachment from the later scarp, while the lower block movements needed to be analysed in detail to assess the damming potential (also in comparison with the present situation).
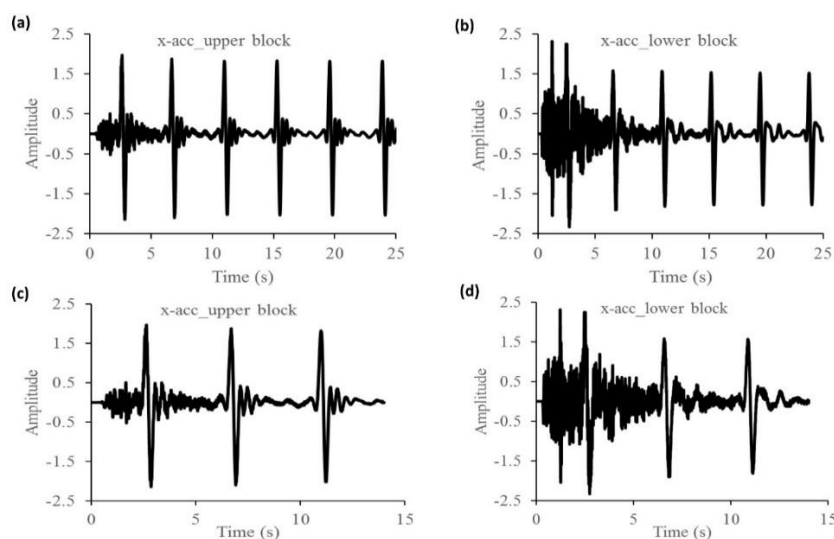
Figure 8. X-acceleration for 25 (a, b) and 14 (c, d) seconds computational time. Accelerations labelled as 'xacc_lower block' and 'xacc_upper block' correspond respectively to history points 15 and 12 mentioned in Fig. 6.

Table 3. PGA and Ia measured along the profile for the 14 and 25 seconds in the bedrock, in the upper block (point 12*), in the middle block (point 13*) and in the lower block (point 15*).

Location	Duration=14sec		Duration=25sec	
	PGA, (m s^{-2})	Ia (m s^{-1})	PGA (m s^{-2})	Ia (m s^{-1})
Rock	1.99	0.55	1.99	0.28
12*	1.97	0.95	1.97	0.48
13*	2.24	1.05	2.24	0.55
15*	2.42	0.91	2.31	0.52

Regarding the main landslide triggering factors, this was assessed by analysing the calculated safety factor. Scenarios were
220 simulated to highlight the intrinsic behaviour of the model under different loading conditions. First this was fulfilled in the
absence of water and seismic loads. Then, groundwater was added to the model and a seismic input was used. The groundwater
data were recorded along the sliding surface with an x-increment of 10 meters. Results of the safety analysis was completed
for different hydrogeological conditions.

Dry and non-seismic models are assumed to be much more stable. Therefore, scenarios have been made to track the limits
225 from which instability begins. Our discussion is based on the results of the safety factor obtained for a cohesion of 0.01 MPa
and 0.02 MPa and for friction angles of 15 °, 17 ° and 20 ° as summarized in Table 4.

Table 4. Safety factor obtained for a cohesion of 0.01 MPa and 0.02 MPa for different friction angles (G1=dry and non-seismic; G4 is
seismic and saturated). Scenarios involving groundwater and seismic shaking considered a complete saturation of the sliding layers
(additional GWT5 scenario) and a wavelet of 25s shaking time. G4a and G4b correspond to the partial and complete saturation.

Joint cohesion (MPa)	Joint Fric. angle (°)	Safety factor/G1 (-)	Safety factor/G4a (-)	Safety factor/G4b (-)	Ratio $\dfrac{G1}{G4a}$	Ratio $\dfrac{G1}{G4b}$
	15	1.59	0.89	0.81	1.79	1.96
0.01	17	1.68	1.03	0.91	1.63	1.85
	20	2.23	1.22	1.09	1.83	2.05
0.02	17	1.75	1.05	0.95	1.67	1.84

230

As expected, those results in Table 4 show a strong dependence of the Factor of Safety (FoS) of the slope on the friction angle
of the slope material. Furthermore, we notice that the FoS of the slope for dry and non-seismic scenarios is almost twice larger
than the safety factor corresponding to saturated and seismic conditions. Actually, in the absence of water and seismic
vibration, the initial slope of the Banana Tree landslide site would have been stable unless very (and unrealistically) low values
235 of cohesion and friction angle are considered (e.g. friction angle of less than 10°). This confirms our first estimates of the
important role of groundwater pressures and seismic vibrations with respect to the slope destabilization. Based on the local
and regional context, other environmental and anthropogenic parameters were identified as factors that have contributed to the
increase of field stresses, forcing the landslide triggering and evolution. These factors are: earthquakes, erosion at the slope
toe (fluvial erosion and quarrying) and upper slope overloading due to the installation of the inhabitants. The last also causes
240 other effects like the vegetation removal and galleries due to some cultural technics which can evolve to a favourable situation
to landslide triggering under heavy rain context. This is in line with steps of the process leading to slope instability and landslide
triggering as described by Terzaghi (1950), Varnes (1978), Popescu (1994) and Popescu (2002). Moreover, the general north-
south direction of the layers could have contributed much to the process amplification. As illustrated in Fig. 14a, the layers are
parallel to the direction of the sliding, this allows easy movements downwards in case of even small slope destabilization.

245 **3.2 Analysis of the actual state of stability and potential x-displacement**

After the back-analysis, simulations of the current situation of the landslide were computed to study the present landslide state
of stability**.** In this section, we have focused on a displacement-oriented analysis, as the main purpose is the study of the
conditions under which the landslide could form a dam.The results given in Fig. 9 and Table 5 constitute the basis for this
analysis. Large PGA and Ia are observed at the lower (and thicker) block of the landslide. This difference is also observed for
250 the values and the distribution of the x-accelerations during the shaking time, again with high values for the downstream block.
This difference will also affect the disproportionate horizontal x-displacements of the blocks, creating extension and
compression zones. Extension zones can lead to the opening of large cracks.

Table 5. PGA and Ia in the profile for the 14 and 25 seconds. Locations 12*, 13* and 15* refer to the upper, the middle and the lower bloc, as mentioned in Fig. 5

Location	Duration=14sec		Duration=25sec	
	PGA, (m s^{-2})	Ia (m s^{-1})	PGA (m s^{-2})	Ia (m s^{-1})
Rock	1.97	0.30	1.90	0.57
12*	3.34	1.08	2.04	0.71
13*	2.12	0.52	2.10	1.32
15*	4.24	1.17	2.45	1.10

255
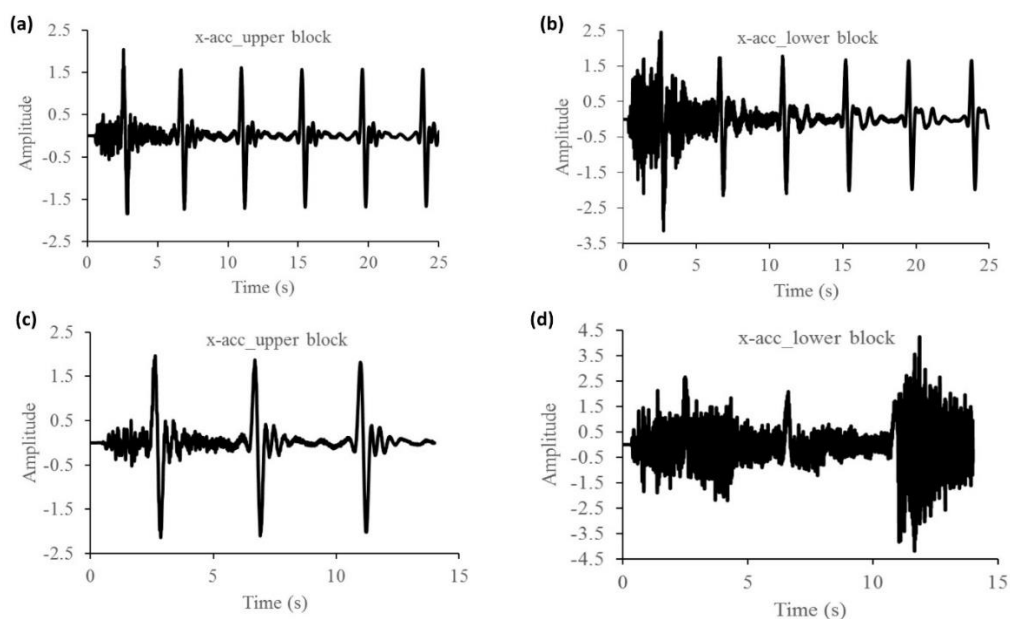
Figure 9. Actual- X-acceleration for 25 seconds (a, b) and 14 seconds (c, d) computational time.
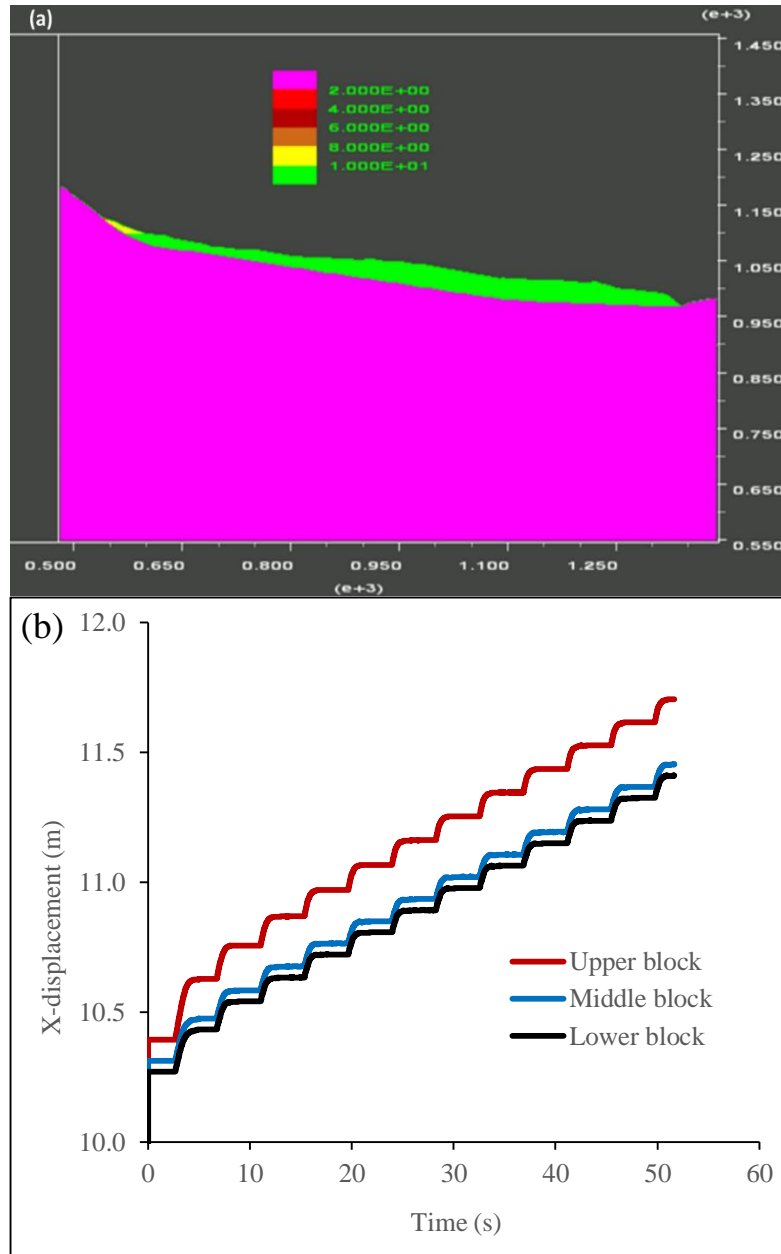
Figure 10. Plots of blocks (a) and displacements (b) as given in the UDEC output for run 13 (see Fig. A1b: using a cohesion of 0.01 MPa and a seismic shaking of 20 seconds).

Figure 10 describes the landslide situation after scenario 13 (detailed in Fig. A1b), showing that increasing the shaking duration would result in displacement increase over 12 m. The model sometimes provided disproportionate displacements between the three main blocks (Fig. 10b). This leads to compression and shear zones between the blocks and would even probably be the main cause of the spurts of ground water to form the small lakes hanging up the Kanyosha River.

Table 6. The role of water in the model behaviour. Values are based on recorded displacements under scenario 9, 10, 11, 14, 16 and 17.

	Friction angle=11° t=25 S, c=0.01 $\dfrac{saturated}{Dry}$	Friction angle=15° t=25 S, c=0.01 $\dfrac{saturated}{Dry}$	Friction angle=17° t=25 S, c=0.01 $\dfrac{saturated}{Dry}$
Xdis_UPPER Bloc	14.2	7.8	3.0
Xdis_LOWER Bloc	5.1	2.4	2.9

The results of this Table 6 show the effects of water on the dynamics of the Kanyosha landslide. Under certain conditions of cohesion and shaking duration, the presence of water X-displacement increases by 2.4 to 14 times. Kainthola et al. 2012 found a change of 79.1 %, corresponding to an increase of approximately 1.8 times. This explains why many cases of reactivation or acceleration of landslides occur during rainy periods. These results are discussed with more detail in section 4.1. A full river blockage is possible. Actually, it is likely that the displacements would have been larger for stronger shaking and if we had also modelled plasticity within the blocks. Furthermore, we must consider that some destabilisation mechanisms cannot be computed with UDEC, such as fluidisation or liquefaction of the clayey landslide material, which would produce much larger displacements.

3.3   Effects of the dam breaching on flood hazard

3.3.1 Water depth

In this section, we examine to which extent the water depths are affected by the occurrence of a landslide dam breaching. As it is not possible to anticipate when the breaching might occur, we consider three different pre-failure flow conditions (base flow, 20-year flood and 50-year flood). The computed water depths are reported here for four cross-sections, labelled sections 1 to 4 (Fig. 3).

Figure 11 displays the computed water depths for the pre-failure flow and for the breach-induced flow, for section 1 to 4, considering a roughness height of 0.1 m (Fig. 11a) and 0.3 m (Fig. 11b). For the base flow scenario and for both values of k_s, the computed water depth in section 1 is about 23 times higher when dam breaching is taken into account compared to a base flow situation without dam breaching. This value is reduced to about 5.5 and 3.5 respectively for pre-failure flow conditions corresponding to a 20- and a 50-year flood. Similarly, the increases in water depths induced by the dam breaching become more moderate for sections 2, 3 and 4 which are located respectively at about 2, 4 and 6 km downstream of the dam.

These results show that dam breaching aggravates considerably the flood conditions in the downstream river. This conclusion remains robust despite the high uncertainties on the roughness parameter. Indeed, as shown in Tab. 7, changing the roughness has little influence on the relative effect of dam breaching on the water depths. This is also confirmed by the high similarity between Figs. 11a and 11b.
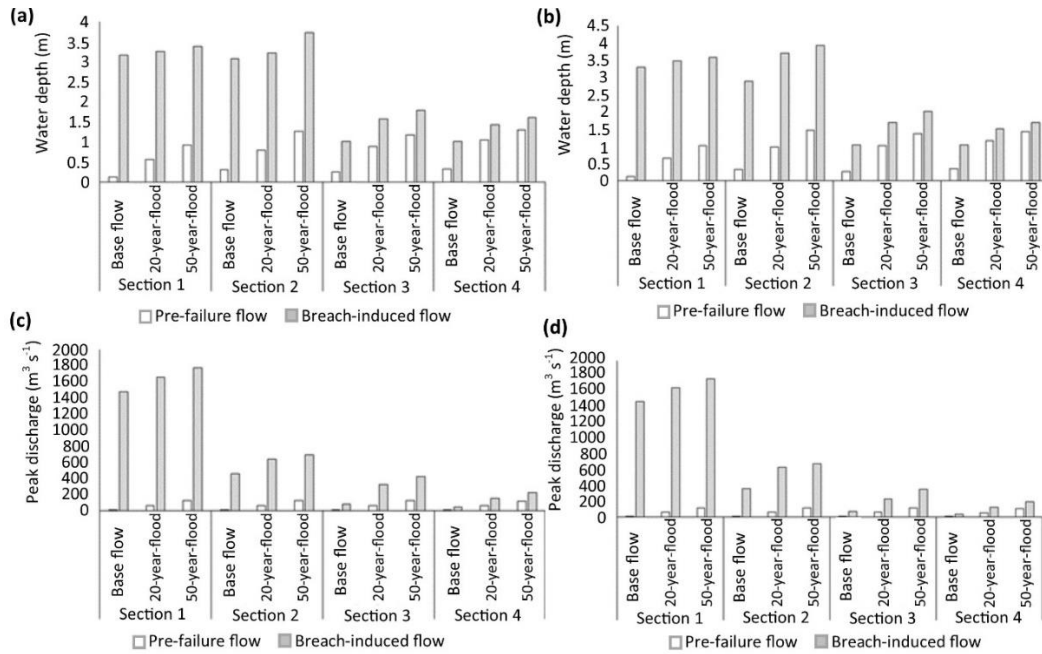
Figure 11. Computed water depths (a, b) and discharge (c, d) for various pre-failure flow conditions (base flow, 20- and 50-year floods), and corresponding maximum water depths (a, b) and peak discharges (c, d) after dam breaching, in cross-sections 1 to 4 and for a roughness height $k_s = 0.1$ m (a, c) and 0.3 m (b, d).

Table 7. Ratio between the maximum water depth following dam breaching and the water depth in the pre-failure flow conditions in sections 1 to 4, considering two different roughness heights ($k_s = 0.1$ m and $k_s = 0.3$ m) and various pre-failure flows (base flow, 20-year flood and 50-year flood).

	Section 1		Section 2		Section 3		Section 4	
k_s (m)	0.1	0.3	0.1	0.3	0.1	0.3	0.1	0.3
Base flow	22.6	23.5	9.6	8.5	3.8	3.8	3.1	3.0
20-year flood	5.7	5.3	4.0	3.7	1.8	1.7	1.4	1.3
50-year flood	3.6	3.5	2.9	2.7	1.5	1.5	1.2	1.2

3.3.2 Peak discharge

The peak discharge of the flood waves induced by dam breaching are in the ranges 1500 -1700 m³ s⁻¹, 460-580 m³ s⁻¹, 77-300 m³ s⁻¹ and 41-110 m³ s⁻¹ in sections 1, 2, 3 and 4 respectively (Figs. 11c and 11d). In the uppermost section (n°1), which is located close to the toe of the dam, the roughness height has virtually no influence on the computed peak discharge as the flow in this area is predominantly controlled by the dam failure. In contrast, the peak discharge is gradually more influenced by the roughness height as the flood wave propagates towards the more downstream cross-sections 2, 3 and 4.

In cross-section 1, the peak discharge of the dam-breaching flood wave is roughly 500 times higher than the base flow, 30 times larger than a 20-year flood and 15 times larger than a 50-year flood (Tab. 8). In the more downstream cross-sections, these numbers become smaller; but the peak flow after dam breaching remains at least two to ten times larger than typical

flood discharges (20- or 50-year floods) and can be 100 times larger than the base flow in the river. These results are only slightly affected by a change in the roughness height.

We find again that neglecting dam failure would result in a strong underestimation of the downstream flood hazard. This underestimation is particularly severe in the cross-sections located close to the dam, whereas in the more downstream area, this effect is mediated by peak flow attenuation during wave propagation.

Table 8. Ratio between the peak discharge following dam breaching and the discharge in the pre-failure flow conditions in sections 1 to 4, considering two different roughness heights (k_s = 0.1 m and k_s = 0.3 m) and various pre-failure flows (base flow, 20-year flood and 50-year flood).

	Section 1		Section 2		Section 3		Section 4	
k_s (m)	0.1	0.3	0.1	0.3	0.1	0.3	0.1	0.3
Base flow	490	490	150	120	27	25	15	14
20-year flood	28	28	11	11	5.4	3.8	2.6	2.2
50-year flood	15	15	5.7	5.7	3.5	2.9	2.0	1.8

3.3.3 Wave propagation time

Figure 12 displays the wave propagation time in sections 1 to 4, i.e. the time elapsed between the dam failure and the moment the flood wave reaches the corresponding section of the river. The time-to-peak, i.e. the time between the dam breaching and the arrival of the peak discharge in the corresponding river sections is also displayed. Results are shown for two roughness heights, k_s = 0.1 m and k_s = 0.3 m.

In the upper part of the river, the wave propagation time remains mostly independent of the pre-failure flow. The flood wave takes between 2.5 and 3 min to reach section 2, which corresponds to a wave velocity of the order of 10 to 12 m s^{-1}. Further downstream (urbanized area), the pre-failure flow has a strong influence on the wave propagation velocity. When the pre-failure conditions in the river correspond to base flow, the wave takes roughly 12 min to reach section 3 and 25 min to reach section 4. These values drop to 7-8 min and 12-14 min if the dam breaching takes place during a river flood, corresponding to a rise in the mean wave velocity from 4-6 m s^{-1} in base flow conditions up to 7-9 m s^{-1}.

Hence, the higher the pre-failure discharge in the river, the shorter the wave propagation time and time-to-peak. Compared to a dam failure occurring when the river discharge is low (base flow), the wave propagation time and time-to-peak are approximately reduced by a factor two if the failure occurs during a flood, which corresponds incidentally to the most likely scenario. Although dam breaching has a relatively weaker influence on maximum water depth and peak discharge when the pre-failure flow corresponds to flood conditions (sections 0 and 0), the results obtained here demonstrate that even in flood situations dam breaching is particularly dangerous because of the shorter time between the occurrence of failure and the wave arrival. Overall, the velocity of the flood wave gives little chance for the population to take precautionary measures such as evacuation; unless the population is very well prepared and some early-warning system can be put in place.

Figure 12 shows also the diffusion of the flood wave as it propagates in the valley. While the difference between the wave arrival time and the time-to-peak is low in sections 1 and 2 (generally below 0.5 min), it reaches 1 to 2 min in section 3 and 2.5 to 4.5 min in section 4. This shows that the flood wave is considerably steeper in the upper part of the valley (sections 1 and 2). Also, the wave remains steeper when dam breaching occurs during a river flood than when it occurs during base flow.

The value chosen for the roughness height has virtually no influence on the computational results in sections 1 and 2, which
345   are relatively close to the dam; whereas it has more influence at sections 3 and 4. Nonetheless, the main observations detailed
above remain valid for both values of the roughness height (k_s = 0.1 m and k_s = 0.3 m).
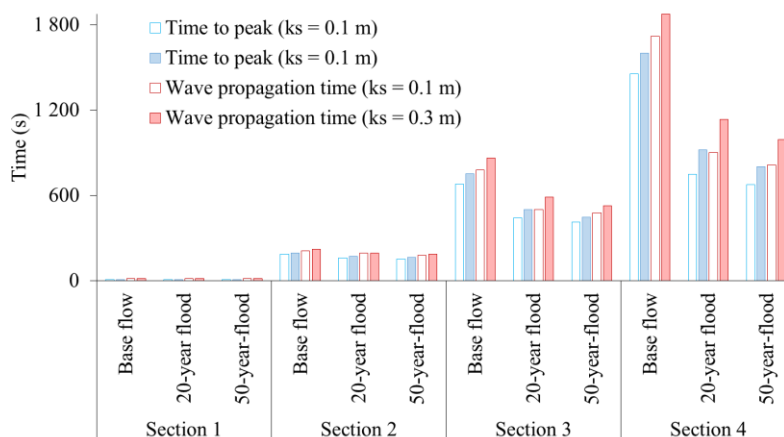
Figure 12. Computed wave propagation time and time-to-peak in sections 1 to 4, for various pre-failure flow conditions (base flow, 20- and
50-year flood) and for two different roughness heights (k_s = 0.1 m and k_s = 0.3 m).

350   **3.4   Floodplain delineation and hazard mapping**

The special floodplain aspects analysed relate mainly to the spatial extension expressed in terms of surface and its variation
for different return periods. For each case, as given in Table 9, values are given for both failure and non-failure scenarios.
Changes induced by the dam failure are also quantified and discussed. Under the same roughness height, both in a failure or a
non-failure situation, the flood extent remains greatly linked to the steady flow discharge. For example, from the base flow to
355   the 50-year flow, the average flood area increase is 25 %, using a roughness height of 0.1 m. This increase is approximately
16 % from the base flow to the 20-year steady flow. These ratios remain almost constant both in the failure and non-failure
scenarios.

Table 9. Predicted change in terms of flooded area due to the landslide induced dam breaching for roughness=0.1 m.

Pre-failure flow	Pre-failure flooded area (m²)	Maximum flooded area after dam failure (m²)	Relative increase in flooded area as a result of dam breaching (%)
Roughness height k_s = 0.1 m			
Base flow	447660	601184	34.29
20-Year	529204	695236	31.37
50-Year	556816	757300	36.01
Roughness height k_s = 0.3 m			
Base flow	493028	635484	28.89

| 20-Year | 604988 | 741964 | 22.64 |
| 50-Year | 747764 | 898048 | 20.10 |

360   The floodplain extent variations are also linked to the roughness changes. For pre-failure scenarios, from a height of 0.1 m to 0.3 m, the surface of the floodplain increases by 10 %, 14 % and 34 % for the base flow, the 20-year and 50 years of return period. In case of the dam breaching, these increases are 6 %, 7 % and 19 %.
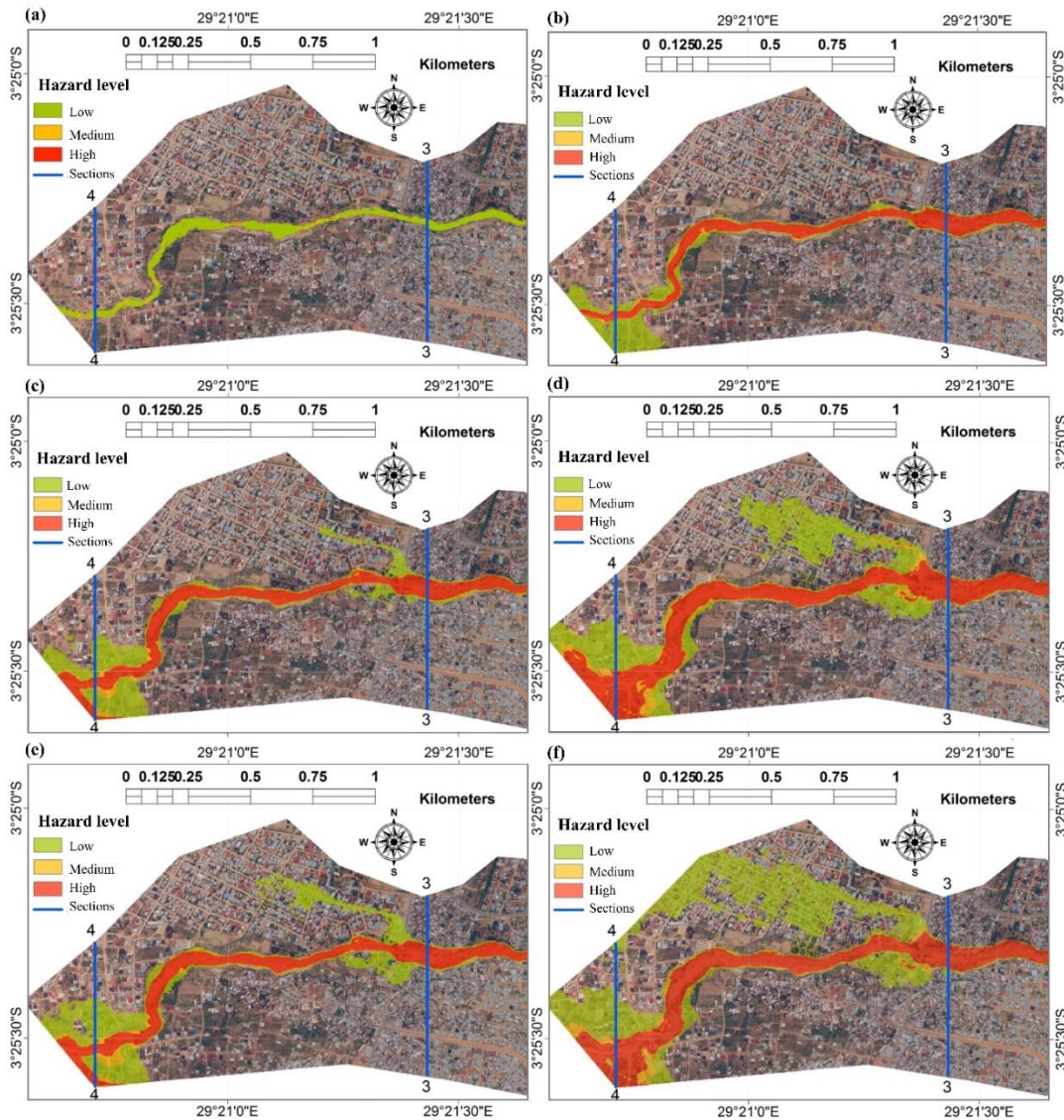
Figure 13. Hazard maps for different initial steady discharges and roughness: base flow in a pre-failure (a) and in a failure (b) case with
365   roughness height of 0.1 m; a 50-year flow in a pre-failure (c) and failure (d) case with roughness height of 0.1 m; a 50-year flow in a pre-failure (e) and failure (f) case with roughness height of 0.3 m.

The maps in Fig. 13 show the spatial distribution of the flood hazard. Values are calculated on the basis of the water depth and velocity. Then, they are classified according to the methodology described in Sec. 2.5 above. The hazard mapping shows the impact of the dam failure on the flood hazard. These maps relate to the lower parts of the watershed, between sections 3 and 4 of Fig. 3, in the city of Bujumbura. Maps in the first column (left column) represent the scenarios without dam breaching. Those in the right-hand column relate to the corresponding failure scenarios. Subfigures (a) and (b) relates to pre-failure flow conditions corresponding to base flow, while the subfigures (c) to (d) are related to a pre-failure 50-year flood. The comparison between maps of the first and second rows helps to analyse changes related to the initial flow, while the differences between the second and the third rows are the result of the change in roughness within the bottom of the river. Each time, the maps in the right column highlights changes due to the dam breaching.

The maps in the first row (Figs. 13a and 13b) correspond to the base flow case. Their comparison allows to realize a significant change especially downstream with a lateral extension of the flood hazard. Thus, notable changes are observed and consist of a change in the hazard level. Almost all zones classified in the low level hazard category in the non-failure case migrated directly into the high level hazard category in case of a failure scenario. As for maps on the second-row (Figs. 13c and 13d) simulated on the basis of a 50-year flood, the changes are also remarkable. The vertical comparison between the first two rows highlights the variations of the hazard depending on the initial flow rate, as well as in a failure and in a non-failure case, under a roughness height of 0.1 m. Unlike the previous ones (Figs. 13a and 13b), the no-breach scenario (Fig. 13c) already includes zones under the high-category hazard. However, the lateral extension of the hazard is much more obvious than previously, especially near cross section 3. The corresponding failure scenario (Fig. 13d) shows significant increases in flood hazard both on the south and north river banks. Comparison Figs. 13c and 13d to Figs. 13e and 13f reveals that a higher roughness height increases substantially the estimated flood hazard, due to the corresponding increase in water depth.

4 Discussion

4.1 Comments on the landslide analysis

The main question about the present state of the BTL has already been introduced above: under certain conditions BTL is likely to be destabilized, but is a full blockage of the river possible?

In addition to above modelling results, we present here some direct proofs of the likely future massive activation of the landslide – under certain conditions (similar to the simulated worst-case scenarios). First, many ground cracks as well as rock structures favouring sliding along the slope (Figs. 14a and 14d) were found on the landslide surface and at its foot, respectively. Apart from the fact that these cracks and layers constitute zones of weakness, they contribute to the landslide destabilization by diverting large quantities of the runoff water to the inner part of the landslide and to the main sliding surface. This water can contribute to the lubrication of the clay that may then form 'soap layers' (see such 'soap layer' surface in Fig. 14b), or by the recharge of the aquifer whose rise leads to the slope instability as shown in in the sections above. Due to the landslide surface morphology, water could accumulate at its surface and form some ponds (see view of main pond in Fig. 14c). Those ponds do not only contribute to the saturation of the soil, but they also constitute an additional active load for sliding. One scenario that could not be simulated includes the opening of fractures below those ponds that would drastically increase the groundwater pressures at depth. All these elements allow us to validate the simulated scenarios considering worst case conditions (high groundwater pressure, seismic activation) and indicate that even much larger movements could occur than those that were modelled: seismic vibrations could contribute to fracture opening, which in turn would allow rapid inflow of surface (and runoff) water, which could result in massive movements of materials. At least, a 15 m-high landslide dam could form: our simulations resulted in such a 15 m-high dam along the river axis – but which did not fully block the river section as the 12 m horizontal displacement would still allow the river to flow around the landslide; larger horizontal displacements such as those expected after pouring of all existing pond waters into the landslide, down to the sliding surface, would probably

result in a full river blockage. Behind this dam a water impoundment of about 60×10^3 m³ or more could develop. For the
410 evaluation of this volume we consider the extension of past lakes that had been dammed by the same landslide as proved by
the presence of lake sediments directly upstream from the landslide (covering a surface area of about 12000 m²).

Figure 14. Field evidence for the critical stability of BTL. (a): View of the vertical stratigraphy at the foot of the landslide, with an overall
orientation of layers from south to north parallel to the sliding direction (red arrow). The upper layers are clearly seen above the bedrock.
415 This also partly shows the river bed granularity; the small stone marked with a red cross to the right side of the blue arrow is about 15 cm.
The blue indicates the river flow direction. (b): View of a crack on the sliding interface in clay. The red arrow shows the direction of sliding
of the right part along the clay layer. (c): Pond on the landslide with an oil palm designated by the white arrow. This shows that these ponds
are recent (oil palm trees do not grow in water; its particular foliage compared to others shows that its growth was stopped recently). (d) A
crack found on the landslide surface.

420 **4.2   Key findings from the hydraulic modelling**

The first key element highlighted by our flood scenario analysis is the influence of the surface roughness on the dynamics of
the Kanyosha River. The studied dam failure scenarios complete the findings of the stationary analysis by providing a better
understanding of the hydrological behaviour of the Kanyosha River. Most importantly we found that, according to the worst
case scenarios, a large flow discharge is expected to arrive very quickly near the inhabited regions, which might not allow the
425 inhabitants to escape. This result is strongly depending on the river bed roughness change, potentially due to previous floods
and/or anthropogenic disturbances. These findings are of a great interest, as they can help decision makers to promote a non-
risky city management near Kanyosha River and other rivers in similar conditions, by controlling all activities that can alter
the roughness of the rivers, knowing their effects on the flood hazard. Hazard maps are good tools showing the areas that can
be affected under different scenarios and helping to take adequate measures to avoid losses due floods. The effects of dam
430 failure on the flood hazard are well highlighted. Significant changes in failure scenarios computed only with base flow

constitute the most important element in risk prevention. Indeed, warning systems are based on data provided by meteorological services analysing the likelihood of heavy rainfall. However, dam failures can produce floods that are several times more severe than those caused by concentrated surface runoff. This shows that dam failure can distort flood forecasts, creating surprises through non expected circumstances. Hence multi-hazard analyses remain of great interest in high geological
435 risk environments such as those found along the East African Rift system.

4.3   Uncertainties and limitations

As there were no data available for defining the river bathymetry, this may obviously be a source of uncertainty affecting the flood scenario simulations. Moreover, strong variations of the characteristic size of the bottom irregularities were found along the river channel. Therefore, even though this was handled by changing the values within the friction parametrization, there
440 are surely still minor errors due to the use of each value for the whole profile.

5   Conclusions

The processes of the triggering and evolution of the Banana Tree landslide along the slope south of the Kanyosha River near Bujumbura were analysed. A large set of simulations was computed to understand how the landslide evolved from its initial
445 situation to the current state by back-analysis. Results showed that the sliding must have been initially triggered under extreme conditions, involving high groundwater pressures and most likely also quite strong seismic shaking. Furthermore, we showed that the Banana Tree landslide in its present state can still lead to disasters in the future, as the combination of earthquakes and increased groundwater pressures could result in massive downslope movements.

It should be highlighted that the landslide is still active, especially within the downstream block where the river erosion at the
450 foot of the slope and the ground saturation are accelerating sliding processes. Enhancement of those processes (by higher groundwater pressures, possibly also due to seismic shaking, and/or due to ground cracks allowing for rapid surface water infiltration, etc.) will inevitably lead to larger movements and the formation of a landslide dam, behind which a large lake could develop.

A hydraulic model provided valuable quantitative information on the flood wave characteristics and propagation – considering
455 the pre-condition of full dam formation breaks and rapid release of the waters stored behind it after sudden dam collapse. It enabled us to assess quantitatively different failure scenarios as well as the influence of various parameters. One of the most important conclusions of this work is that some areas assumed to be in security with respect to flooding related to simple concentrated surface water runoff might become exposed to extreme flood hazards in case of dam failures. Hence, it is important to take these realities into account in a sustainable spatial management planning and especially in areas marked by
460 high population densities. Flood hazard mapping is still a good tool and can be used as a guide, helping decision makers in urban planning.

465

470 **Appendix A: Scenarios scheme for landslide analysis**
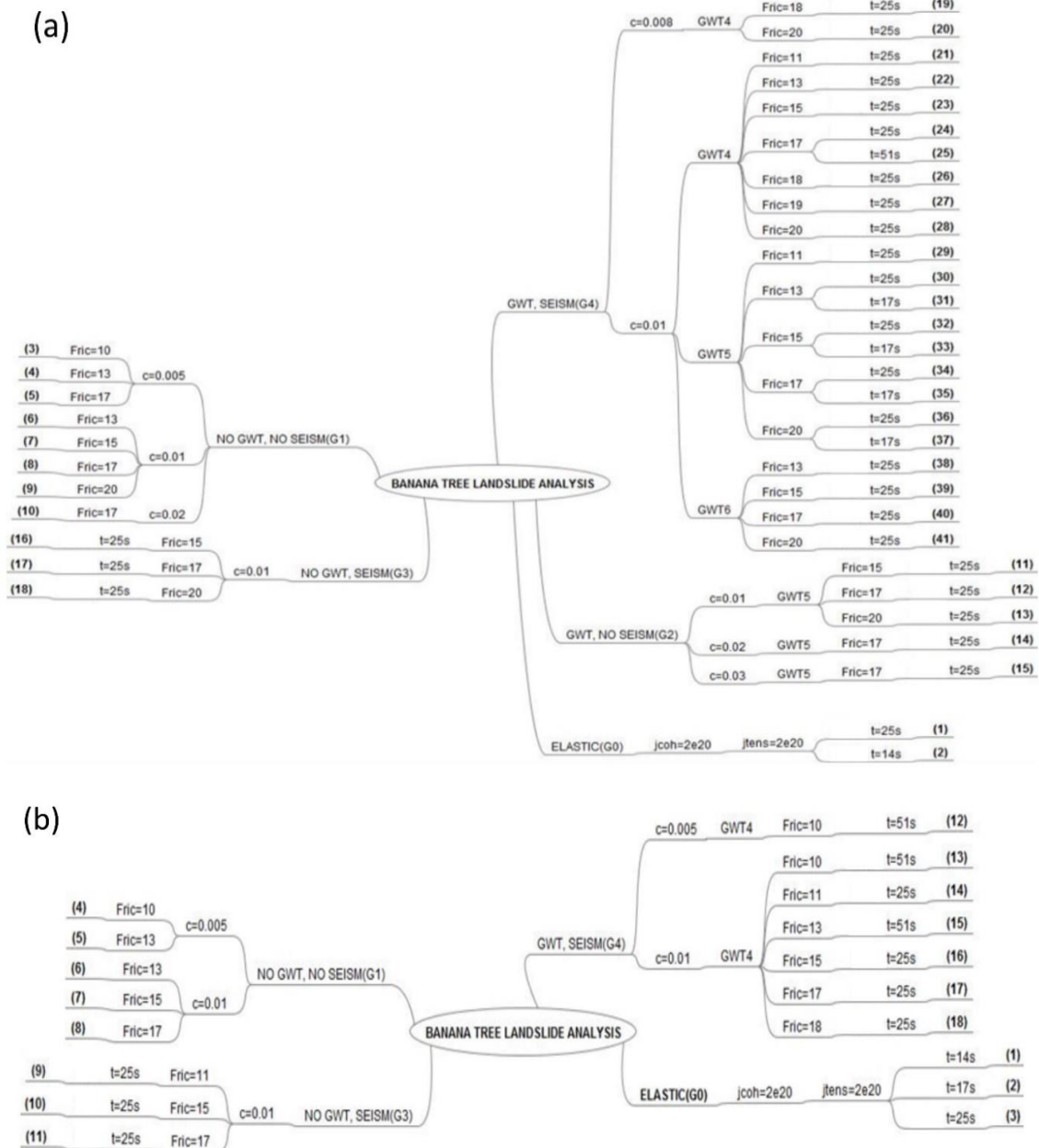
Figure A1. (a) Scenarios for landslide genesis: back analysis (the triggering and evolution up to the actual situation). (b) Landslide stability analysis to simulate possible future evolution. GWT stands for groundwater table, G0 (elastic run made to track the amplification of peak
475 ground acceleration, PGA, and Arias Intensity, Ia, in different parts of the profile), G1 (dry and non-seismic scenarios), G2 (non-seismic and completely or partially saturated scenarios), G3 (dry-seismic scenarios) and G4 (seismic and completely or partially saturated scenarios).

Appendix B: Estimation of flood discharge

The base flow was estimated using Manning equation:

$$Q = \frac{1}{n} A R^{2/3} S^{1/2} \qquad (B1)$$

with n the Manning roughness coefficient, A the river cross section (m^2), R the hydraulic radius (m) and S the water surface
480 slope (m m^{-1}). The Manning equation was largely used to estimate the flow discharge in case of lack of direct measurements
data (Herschy 2009; Jacobs et al., 2016; Lumbroso and Gaume 2012; Moody and Martin 2001).
The flow was estimated during the rainy season measurements at a 6 m wide cross section downstream the landslide at 20 m
in upstream side of the cross section 3 of Fig. 3, with an average water depth of 40 cm. It should be noted that the 6m do not
correspond to the full width of the river. The bottom of the river is not flat and the base flow usually follows one or two
485 branches corresponding to the lower part of the minor bed (Fig. 2c). With a local hydraulic slope of 0.01 m m^{-1} and a Manning
roughness n of 0.041 m$^{-1/3}$s, Eq. (B1) gives an approximate flow of 2.92 m^3 s^{-1}. A value of 3 m^3 s^{-1} was used for base flow in
the computation scenarios. Manning roughness coefficient was estimated based on channel descriptions given by Barnes
(1967).

The steady 20-year and 50-year flows used in the different scenarios were calculated using the rational formula:

$$Q_j = \sum_{k=1}^{j} C_{m,k} i_k A_m \qquad (B2)$$

490 with i_k the rainfall intensity (mm h^{-1}), $C_{m,k}$ the runoff coefficient and A_m each of the contributing surfaces (ha); m is defined as
equal to $j-k+1$. The constant intensity was derived from the Intensity-Frequency-Duration law of Bujumbura provided by the
Geographic Institute of Burundi (IGEBU). Huff (1967) method based was used to approximate the intensity distribution during
the project rainfall event. It was developed based on 291 storms analysis and is applicable for catchments up to 1036 km^2 large.
The method provides 4 distributions according to the quartile in which the rainfall is heaviest. For the case of Bujumbura,
495 calculations based on the 2nd quartile distribution were judged to approximate better the intensity variation, given that the peak
intensity usually occurs in the first 3rd of rainfall duration. Based on Kohler (1951)'s equation on soil saturation index and on
the recent work by Mathlouthi and Lebdi (2010) on the Rain-Runoff relationship, there is no doubt that soil saturation during
storms can be strongly influenced by other previous rainfall events. In a context of rainy season base flow, the use of variable
runoff offers little interest. Hence, a constant runoff coefficient was used. We obtained initial peak flows of 61.6 m^3 s^{-1} and
500 123.4 m^3 s^{-1} for a 20-year and a 50-year flows respectively. Being aware that the use of peak flow corresponds to the extreme
scenario, we used 3 m^3 s^{-1}, 60 m^3 s^{-1} and 120 m^3 s^{-1} for the base flow, 20-year and 50-year initial discharge. This small
decrease can be compensated by the lateral infiltrations as we progress downstream.

Appendix C: Sensitivity to the downstream boundary condition

505 To perform the sensitivity analysis, we considered the 20 scenarios described in Table 10. We mainly tested two pairs of L and
w values:

- in a first configuration (scenarios 1 to 9), the water level at the downstream end of the computational domain depends
  substantially on the flow rate ($L = 35$ m, $W = 0.185$ m);

- in another set of model runs (scenarios 10 to 18), the downstream water level is only weakly influenced by the flow

510   rate ($L = 350 \div 3500$ m, $W = 0.185$ m).

For each of the two types of downstream boundary conditions, we analysed three different roughness heights and considered three different discharges. Finally, we also tested one configuration in which the downstream water level remains independent of the pre-failure discharge in the river; but still varies under transient flow conditions (scenarios 19 and 20). This was tested only for the intermediate bottom roughness. For the 20 scenarios, three values of discharge were considered: base flow, 20-year flood and 50-year flood. In all the tested scenarios, the influence of the downstream boundary conditions did not extend over a distance exceeding about 300 meters from the downstream end of the computational domain.

Table C1. Considered scenarios for the pre-failure flow conditions.

		Scenario ID	Roughness (m)	Flow ($m^3\ s^{-1}$)	L (m)	W (m)
Flow-dependent downstream water level	Relatively smooth bottom	1, 2, 3	0.1	3, 60, 120	35	0.1850
	Intermediate roughness	4, 5, 6	0.2	3, 60, 120	35	0.1850
	Relatively rough bottom	7, 8, 9	0.3	3, 60, 120	35	0.1850
Weakly flow-dependent downstream water level	Relatively smooth bottom	10, 11, 12	0.1	3, 60, 120	$350 \div 3500$	0.2754
	Intermediate roughness	13, 14, 15	0.2	3, 60, 120	$350 \div 3500$	0.2754
	Relatively rough bottom	16, 17, 18	0.3	3, 60, 120	$350 \div 3500$	0.2754
Flow-independent downstream level, except for transients	Intermediate roughness	19	0.2	3	35	1.4088
		20	0.2	60	35	0 .695

Acknowledgements:

Results presented in this paper were obtained in the frame of research funded by the Burundi government who supported the PhD studies of Mr. Leonidas Nibigira and by the Belspo (Belgian Federal Science Policy) project GeoRisCA (2012-2017): Geo-Risk in Central Africa: integrating multi-hazards and vulnerability to support risk management. Elevation and meteorological data were provided by the Geographic Institute of Burundi (IGEBU) and the '*Bureau de Centralisation Geomatique du Burundi'*. Therefore, the authors are grateful to both financial supporters and data providers.

References

Alvarez, M., Puertas, J., Peña, E, and Bermúdez, M.: Two-Dimensional Dam-Break Flood Analysis in Data-Scarce Regions: The Case Study of Chipembe Dam, Mozambique, Water, 9(6), 432, doi: 10.3390/w9060432, 2017.

Arias, A.: A measure of earthquake intensity. In Seismic design for Nuclear Powerplants, R.J. Hansen (ed), MIT Press, Cambridge, Massachusetts, 438-483, 1970.

Arrault, A., Finaud-Guyot, P., Archambeau, P., Bruwier, M., Erpicum, S., Pirotton, M., and Dewals, B.: Hydrodynamics of long-duration urban floods: Experiments and numerical modelling, Natural Hazards and Earth System Sciences, 16(6), 1413–1429, 2016.

Barnes, H.: Roughness characteristics of natural channels. U.S. Geological Survey, Water Supply Paper 1849, 1967.

Beckers, A., Dewals, B., Erpicum, S., Dujardin, S., Detrembleur, S., Teller, J., Pirotton, M., and Archambeau, P.: Contribution of land use changes to future flood damage along the river Meuse in the Walloon region, Natural Hazards and Earth System Sciences, 13(9), 2301–2318, 2013.

Bellon, H. and Pouclet, A. : Datation K-Ar de quelques laves du Rift-Ouest de l'Afrique Centrale : implications sur l'évolution magmatique et structurale, Geol. Rundsch., 69 (1): 49-62, 1980.

Bhasin, R. and Kaynia, A. M.: Static and dynamic simulation of a 700-m high rock slope in western Norway, Engineering Geology, 71(3), 213-226, 2004.

Bruwier, M., Erpicum, S., Pirotton, M., Archambeau, P., and Dewals, B. J.: Assessing the operation rules of a reservoir system based on a detailed modelling chain, Natural Hazards and Earth System Sciences, 15(3), 365–379, 2015.

Chuhan, Z., Pekau, O. A., Feng, J., and Guanglun, W.: Application of distinct element method in dynamic analysis of high rock slopes and blocky structures, Soil Dynamics and Earthquake Engineering, 16(6), 385-394, 1997.

Cundall, P. A.: A computer model for simulating progressive large scale movement in blocky rock system, Paper presented at the Sympo. ISRM., Nancy, France, 1971.

Delvaux, D., Mulumba, J.L., Sebagenzi Mwene Ntabwoba, S., Bondo, S.F., Kervyn, F., and Havenith, H.B.: Seismic hazard of the Kivu rift (western branch, East African Rift system): new neotectonic map and seismotectonic zonation model, Journal of African Earth Sciences, doi: 10.1016/j.jafrearsci.2016.10.004, 2016.

Detrembleur, S., Stilmant, F., Dewals, B., Erpicum, S., Archambeau, P., and Pirotton, M.: Impacts of climate change on future flood damage on the river Meuse, with a distributed uncertainty analysis, Natural Hazards, **77**(3), 1533–1549, 2015.

Dewals, B., Erpicum, S., Detrembleur, S., Archambeau, P., and Pirotton, M.: Failure of dams arranged in series or in complex, Natural Hazards, 56(3), 917–939, 2015.

Ernst, J., Dewals, B. J., Detrembleur, S., Archambeau, P., Erpicum, S., and Pirotton, M.: Micro-scale flood risk analysis based on detailed 2D hydraulic modelling and high resolution geographic data, Natural Hazards, 55(2), 181–209, 2010.

Esaki, T., Jiang, Y., Bhattarai, T. N., Maeda, T., Nozaki, A., and Mizokami, T.: Modelling jointed rock masses and prediction of slope stabilities by DEM. In Vail Rocks 1999, The 37th US Symposium on Rock Mechanics (USRMS), American Rock Mechanics Association, 1999.

Field, C.B., Barros, V., Stocker, T.F., Qin, D., Dokken, D.J., Ebi, K.L., Mastrandrea, M.D., Mach, K.J., Plattner, G.-K., Allen, S.K., Tignor, M., and Midgley, P.M. (éds.): Managing the Risks of Extreme Events and Disasters to Advance Climate Change Adaptation, A Special Report of Working Groups I and II of the Intergovernmental Panel on Climate Change (Cambridge and New York: Cambridge University Press), 2012.

Gemenne, F., Blocher, J., De Longueville, F., Perrin, N., Vigil Diaz Telenti, S., Zickgraf, C., Gharbaoui, D., and Ozer, P. : Catastrophes, Changement climatique et Déplacements forcés : Dynamiques régionales de mobilité humaine en Afrique de l'Ouest, Nansen Initiative, 30 pp, 2014.

Herschy, R.: Streamflow measurement, 3rd edn, Taylor and Francis, New York, 2009.

Huff, F. A.: Time distribution of rainfall in heavy storms, Water Resources Research, 3 (4), 1007-1019, 1967.

Ilunga, L. : Etude des sites majeurs d'érosion à Uvira (R.D. Congo), Geo-Eco-Trop, 30 (2) : 1-12, 2006.

570   Jacobs, L., Maes, J., Mertens, K., Sekajugo, J., Thiery, W., Van Lipzig, N., Poesen, J., Kervyn, M., and Dewitte, O.:
           Reconstruction of a flash flood event through a multi-hazard approach: Focus on the Rwenzori Mountains, Uganda,
           Nat. Hazards, 84(2), 851–876, doi:10.1007/s11069-016-2458-y, 2016.

       Kainthola, A., Singh, P.K., Wasnik, A.B., Sazid, M., and Singh, T.N.: Distinct element modelling of Mahabaleshwar road cut
           hill slope, Int J Geomaterials. 2:105–113, 2012.

575   Kohler, M. A. and Linsley, R. K.: Predicting the runoff from storm rainfall, Washington DC: Weather Bureau, US Dept of
           Commerce, Research Paper 34, 1951.

       Kveldsvik, V., Kaynia, A. M., Nadim, F., Bhasin, R., Nilsen, B., and Einstein, H. H.: Dynamic distinct-element analysis of the
           800m high Åknes rock slope, International journal of rock mechanics and mining sciences, 46(4), 686-698, 2009.

       Lumbroso, D. and Gaume, E.: Reducing the uncertainty in indirect estimates of extreme flash flood discharges, J Hydrol 414–
580   415:16–30, doi:10.1016/j.jhydrol.2011.08.048, 2012.

       Machiels, O., Erpicum, S., Archambeau, P., Dewals, B., and Pirotton, M.: Theoretical and numerical analysis of the influence
           of the bottom friction formulation in free surface flow modelling, Water SA, 37(2), 221–228, 2011.

       Mathlouthi, M. and Lebdi, F. : Modélisation de la relation pluie-ruissellement par durée d'épisode pluvieux dans un bassin du
           nord de la Tunisie, Hydrological Sciences Journal, 55 :7, 1111-1122, doi : 10.1080/02626667.2010.512471, 2010.

585   Moeyersons, J., Trefois, P., Nahimana, L., Ilunga, L., Vandecasteele, I., Byizigiro, V., and Sadiki, S.: River and landslide
           dynamics on the western Tanganyika rift border, Uvira, DR Congo: diachronic observations and a GIS inventory of
           traces of extreme geomorphologic activity, Natural hazards, 53(2): 291-311, 2010.

       Moody, J.A. and Martin, D.A.: Post-fire, rainfall intensity-peak discharge relations for three mountainous watersheds in the
           Western USA, Hydrol Process 15:2981–2993, doi:10.1002/hyp.386, 2001.

590   Popescu, M.E.: Landslide causal factors and landslide remedial options, Proc. 3rd Int. Conf. Landslides Slope Stability and
           Safety of Infra-Structures, pp. 61-81, 2002.

       Popescu, M.E. and Yamagami, T.: Back Analysis Of Slope Failures - A Possibility Or A Challenge?, Proc. 7th Intern. IAEG
           Congress, Lisbon, 4737-3744, 1994.

       Reliefweb: Burundi: Floods and Landslides - Feb 2014, available at: http://reliefweb.int/disaster/fl-2014-000019-bdi
595   (Accessed 21 November 2016), 2014.

       Roger, S., Dewals, B. J., Erpicum, S., Schwanenberg, D., Schuttrumpf, H., Kongeter, J., and Pirotton, M.: Experimental and
           numerical investigations of dike-break induced flows, Journal of Hydraulic Research, 47(3), 349–359, 2009.

       Sharma, L.K., Umrao, R.K., Singh, R., Ahmad, M., and Singh, T.N.: Stability Investigation of Hill Cut Soil Slopes along
           National Highway 222 at Malshej Ghat, Maharashtra, Journal Geological Society of india, Vol.89, 165-174, 2017.

600   Singh, P.K., Wasnik, A.B., Kainthola, A., Sazid, M., and Singh, T.N.: The stability of road cut cliff face along SH-121: a case
           study, Nat. Hazards, 68(2), 497-507, 2013.

Terzaghi, K.: Mechanisms Of Landslides, Geological Society of America, Berkley, 83-123, 1950.

Umrao, R.K., Singh, R., Ahmad, M. and Singh, T.N.: Stability analysis of cut slopes using continuous slope mass rating and kinematic analysis in Rudraprayag district, Uttarakhand, Geomaterials, Vol.1, 79-87, 2011.

605   UNITAR / UNOSAT: Storm damage, Kinama/Kamenge. Areas of Bujumbura, Burundi, available at: http://reliefweb.int/map/burundi/storm-damage-kinamakamenge-areas-bujumbura-burundi-17-february-2014 (Accessed 21 November 2016), 2014.

Varnes, D. J.: Slope movement types and processes, In Schuster, R.L., Krizek, R.J. (Eds) Landslides, Analysis and Control, Special report 176: Transportation Research Board, National Academy of Sciences, Washington, D. C., 11-33, 1978.